UC San Diego

UC San Diego Previously Published Works

Title

Orbital forcing of the East Antarctic ice sheet during the Pliocene and Early Pleistocene

Authors

Patterson, MO
McKay, R
Naish, T
et al.

1 **Response of the East Antarctic Ice Sheet to orbital forcing during the Pliocene and early**

2 **Pleistocene**

3

4 Patterson, M. O.[1]*, McKay, R.[1], Naish, T.[1], Escutia, C.[2], Jimenez-Espejo, F. J.[3, 4], Raymo,

5 M[5]., Tauxe, L.[6], Brinkhuis, H.[7], and IODP Expedition 318 Scientists

6   1) Antarctic Research Centre, Victoria University of Wellington, Wellington, New

7   Zealand

8   2) Instituto Andaluz de Ciencias de la Tierra, CSK – University of Granada,

9   Granada, Spain

10   3) Department of Earth and Planetary Sciences, Graduate School of Environmental

11   Studies, Nagoya University, Nagoya, Japan.

12   4) Institute of Biogeosciences, Japan Agency for Marine-Earth Science and

13   Technology, Yokosuka, Japan.

14   5) Lamont-Doherty Earth Observatory of Columbia University

15   P.O. Box 1000, 61 Route 9W, Palisades, NY, 10964

16   6) Scripps Institution of Oceanography, La Jolla, CA 92093-0220, USA

17   7) Marine Palynology and Paleoceanography, Laboratory of Paleobotany and

18   Palynology, Utrecht University, Budapestlaan 4, 3584 CD Utrecht, NL

19

20   *Corresponding author: molly.patterson@vuw.ac.nz

21

22 **Geological reconstructions of global ice volume[1] and sea-level[2] during the Pliocene and**

23 **Early Pleistocene (5 to 2 Ma) display regular glacial-interglacial cycles occurring every**

24 **41-kyrs, paced by variations in Earth's axial tilt (obliquity). The absence of a strong**

25 **~20-kyr precession signal challenges our fundamental understanding of how ice sheets**

respond to orbital forcing because precession should impart the greatest influence on high-latitude summer insolation intensity, and therefore polar ice volume[3,4]. While a number of hypotheses have been proposed[4,5,6], reconciliation of this conundrum remains hampered by a lack of observational evidence from the Antarctic ice sheet. Here, we present an orbital-scale time-series of ice-berg rafted debris and continental rise sedimentation from a well-dated sediment core (Integrated Ocean Drilling Program site U1361) adjacent to the Wilkes Land margin of the East Antarctic Ice Sheet (EAIS). Our data reveal ~40-kyr cyclic variations in the extent of the EAIS paced by obliquity between 4.3-3.3 Ma during the warmer-than-present climate of the Pliocene, as has previously been demonstrated for the West Antarctic Ice Sheet (WAIS)[7,8]. Under a warmer climate state, mean annual insolation (paced by obliquity) had more influence on Antarctic ice volume, than insolation intensity modulated by precession[6]. However, a transition to 20-kyr precession cycle dominance at 3.3 Ma preceded the development of a more stable EAIS marine margin at ~ 2.5 Ma, reflecting the declining influence of oceanic forcing as the high latitude southern ocean cooled and a perennial summer sea-ice field developed[9]. Our data shows that precession-paced EAIS variability occurs during cold climate states, even when the obliquity signal dominates globally-integrated proxy records, lending support to the hypothesis that anti-phased polar ice-volume cancels out on a precession time scale[4].

A new marine sediment core (U1361) recovered by the Integrated Ocean Drilling Program (IODP) from ~3000 m water depth on the continental rise adjacent to the Wilkes Land sector of Antarctica (Fig. 1; Extended Data Fig. 1) provides a well-dated and continuous geological archive of Pliocene and Early Pleistocene orbital scale variability of the marine margin of the EAIS. Sediment deposition at this site is controlled by the interplay between: (i) downslope marine sediment gravity flows triggered by the buildup of sediment

51 on the edge of the continental shelf during glacial advance; (ii) the rainout of biogenic

52 detritus from surface water plankton; (iii) iceberg rafting of terrigenous sediments and (iv)

53 low energy bottom currents (Supplementary Information).

54   The core consists of eighteen sedimentary cycles spanning an age range of 4.3-2.2 Ma,

55 and comprising alternating terrigenous massive to laminated muds and diatom-rich/bearing

56 silty muds units (cycles 1-18 Fig. 2; Extended Data Fig. 2, 3). In places the muds contain

57 packages of well-defined laminae and are consistent with established models of non-erosive

58 overbank hemipelagic deposition onto a channel levee setting via turbidites on the lowermost

59 Antarctic continental rise[10]. Steeply dipping, seaward prograding wedge sediments are

60 evident in seismic reflection profiles across the continental shelf and extend onto the upper

61 continental slope above seismic unconformity WL-U8 (~4.2 Ma)[11,12] (Extended Data Fig. 1).

62 The geometry of these strata is characteristic of grounding zone deposition by repetitive

63 advances of a marine based ice sheet to the shelf edge during glacial periods[12]. Sediment

64 overloading near the shelf break at submarine canyons heads, in turn triggers turbidity

65 currents down slope channels and leads to overbank deposition at the core site. Low density

66 turbidity currents in overbank "distal" channel level environments on Antarctic continental

67 rise are typically non erosiove[10] (Supplementary Information). Thus, turbidite units are

68 associated with periods of glacial advance to the Wilkes Land continental shelf edge, whereas

69 bioturbated, diatom-rich/bearing facies represent warm interglacial periods of relatively ice-

70 free ocean and increased primary productivity when the grounding line had migrated

71 landward away from the shelf edge. Increased productivity during interglacial warm climates

72 may be associated with enhanced upwelling of nutrient-rich Circumpolar Deepwater

73 (CDW)[13] (Supplementary Information), which has been linked to southward expansion of the

74 westerly wind field in response to a reduced pole-equator temperature gradient during past

75 warm periods[14]. Presently this relatively warm nutrient-rich CDW upwells to the surface

76 north of the Southern Boundary Front of the Antarctic Circumpolar Current and is marked by

77 areas of enhanced productivity immediately to the north of Site U1361 (Fig. 1).

78   We have developed a high-resolution record (~3-4 kyr sample spacing) of ice-berg

79 rafted debris (IBRD) mass accumulation rates (MAR) and opal deposition for the U1361 core

80 (Methods; Extended Data Table 1; Extended Data Fig. 4). Our age model is based on

81 biostratigraphy used to constrain the interpretation of a magnetic polarity stratigraphy[11], and

82 for our initial spectral analysis we have assumed constant, long-term (millennial-scale)

83 sedimentation rates between polarity reversal tie points (Methods; Extended Data Fig. 5).

84   In general the highest intensity of IBRD occurs during transitions from glacial

85 terrigenous mud facies to interglacial diatom-rich/bearing muds up-core until ~47 mbsf, with

86 most IBRD peaks immediately preceding opal peaks (Fig. 2). Isotopic Nd and Sr provenance

87 indicators suggest that the terrigenous components in these diatom-rich/bearing muds are

88 associated with periods of deglacial retreat of the ice margin back into the Wilkes Land

89 subglacial basin during the Early Pliocene[15]. As the Antarctic ice sheet loses the majority of

90 its mass via icebergs[16], we interpret the maxima in IBRD MAR to be the consequence of

91 accelerated calving during glacial retreat from marine terminating outlet glaciers along the

92 Wilkes Land coastline as well as a contribution from EAIS outlet glaciers entering the

93 western Ross Sea (Methods; Supplementary Information). This interpretation is consistent

94 with models and paleo-observations, which imply the most rapid mass loss of the EAIS

95 margin during the last glacial termination occurred between 12-7 ka, and was primarily the

96 consequence of oceanic warming[17].

97   Spectral analysis of the un-turned IBRD MAR time-series displays a dominant period

98 of ~40-kyr between ~4.3-~3.4 Ma, which transitions to strong variance at ~20-kyr periods

99 after ~3.3Ma, with a corresponding decrease in power of the ~40-kyr cycle between 3.3-2.2

100 Ma (Fig. 2h, 2i; Extended Data Fig. 6). On the basis of this strong orbital relationship

101 displayed in frequency spectra of the untuned IBRD MAR time series (Fig. 2), an

102 independent age model, and near continuous and uniform long-term sedimentation (Extended

103 Data Fig. 5), we establish a graphical one-to-one correlation between cycles in ice margin

104 variability expressed by our IBRD data and orbitally-paced climatic time series. Between 4.3-

105 3.3 Ma there is a very strong correlation between 41-kyr cycles mean annual insolation and

106 the benthic $\delta^{18}O$ global ice volume record[1], whereas, between 3.3-2.2 Ma IBRD cycles

107 correlate with the ~20-kyr cycles of summer insolation at 65°S (Fig. 2). We acknowledge that

108 although our visual correlations are constrained by 7 precisely-dated paleomagnetic reversals,

109 they may not represent a unique solution, but as noted above they are entirely consistent with

110 the variance in orbital frequencies implied by our spectral estimations. We then used the

111 graphical relationships in Fig. 2 to explore the role of longer-period orbital influences on the

112 pattern of iceberg calving (Online Methods; Supplementary Information). The top of the ~40-

113 kyr-dominated interval is marked by a ~300-kyr-long condensed section between ~3.6-3.3

114 Ma (Fig. 2; Extended Data Fig. 5), and corresponds to a +1‰ glacial $\delta^{18}O$ excursion

115 spanning Marine Isotope Stage (MIS) MG9 and MIS M2. Indeed, this glacial excursion has

116 also been associated with southern high-latitude climate cooling and the re-establishment of

117 grounded ice on middle to outer continental shelf in the Ross Sea following a ~200-kyr

118 period of warm open ocean conditions[7,9]. Previous studies of older Oligocene and Miocene

119 $\delta^{18}O$ glacial excursions have proposed a relationship between intervals of increased glacial

120 amplitude in the $\delta^{18}O$ record with a coincidence of 1.2 Ma nodes in obliquity and 400-kyr

121 minima in long period eccentricity[18,19]. This orbital configuration, which favours extended

122 periods of cold summers and low seasonality is considered optimal for Antarctic ice sheet

123 expansion, and occurs at ~3.3 Ma - the time of the transition from ~40-yr to ~20-kyr

124 dominance in the IBRD MAR times series from U1361 (Fig. 2).

125   We developed orbital-tuning strategy based on the strong orbital signal in our un-tuned

126   IBRD MAR record, and the clear link between peaks and troughs in austral summer

127   insolation, IBRD MAR and opal content which are synchronous across that top and bottom

128   Kaena Subchron paleomagnetic reversals, respectively (Fig. 3a, and discussed below). Band-

129   pass filters at obliquity and precession frequencies applied to the IBRD MAR confirm visual

130   observations that long-term minima are associated with (eccentricity-modulated) nodes in

131   precession after 3.3 Ma, and the obliquity node at 4.1 Ma (Fig 3b; Extended Data Fig. 7).

132   Observed ~20-kyr-duration IBRD cycles correlated with summer insolation calculated

133   for 65°S for the interval of the core between 3.3-2.2 Ma (Fig. 2; Fig. 3a), are embedded

134   within 100-kyr-duration IBRD cycles (Fig. 2i), with broad peaks of IBRD maxima associated

135   with transitions between laminated mudstones to diatom-rich/bearing muds (Fig. 2b).

136   Although this lithological variability is also evident in frequency spectra of opal percentage,

137   it is not significant at 90% (Extended Data Fig. 6, 7), which is the likely consequence of a

138   lower signal-to-noise ratio in the opal data (Methods; Extended Data Fig. 8). A dramatic

139   decrease in the amplitude of ~20-kyr IBRD peaks, and a change to lithofacies associated with

140   non-erosive low-energy bottom currents at the core site from ~2.5 Ma is broadly coincident

141   with southern high latitude cooling[9] and the onset of major Northern Hemisphere

142   glaciations[9,20]. We attribute the progressive reduction in calving intensity to cooling and a

143   relative stabilization of the EAIS ice margin. Homogenization of the turbidite sediments

144   during glacial maxima by enhanced bioturbation and bottom current activity is observed and

145   likely reflects increased Antarctic sea ice and polynya-style mixing at this time producing

146   oxygenated high salinity shelf water[9], transferred downslope over Site U1361 to form

147   Antarctic Bottom Water[21] (Supplementary Information).

148   In summary, our correlations of variations in IBRD and opal content with the benthic

149     $\delta^{18}O$ stack and orbital time series (Fig. 2) identify up to sixteen ~40-kyr-duration cycles

150 within six major lithological cycles (cycles 13-18 Fig. 2) during the early Pliocene (4.3-3.3

151 Ma). This is followed by forty-two ~20-kyr-duration cycles, within twelve longer-duration

152 lithological cycles (cycles 1-12 Fig. 2).

153   Although, the marine sediment core recovered by the ANDRILL Program from the

154 Ross Sea region provided the first direct evidence, that advance and retreat of the WAIS

155 margin across the continental shelf was paced by obliquity during the Pliocene prior to ~3

156 Ma[7], sub-glacial erosion surfaces in the ANDRILL core associated with ice advance have

157 raised the possibility of missing cycles, particularly after 3.1 Ma. The continuous U1361

158 record presented here confirms the dynamic in phase response, not only of the WAIS but also

159 the marine margins of the EAIS, to obliquity forcing during the warm Pliocene prior to the

160 onset of southern high-latitude cooling at 3.3 Ma.

161   Geological records[7,9,15] and model simulations[8] of recent and past warm climates both

162 highlight the sensitivity of the marine-based portions of the Antarctic ice sheets to ocean

163 warming, but the mechanism by which the coastal ocean warms and destabilises marine

164 grounding lines in response to obliquity forcing remains elusive. It has been proposed that

165 changes in the intensity and the meridional distribution of mean annual insolation controlled

166 by obliquity may have a profound influence on the position and strength of the Southern

167 Hemisphere zonal westerly winds[7]. Indeed, an aerosolic dust record from the Southern Ocean

168 is dominated by ~40-kyr cycles in iron and leaf-wax biomarkers of prior to ~0.8 Ma[22].

169 Moreover, prior to ~3.3 Ma the southward expansion of the westerly wind-field over the

170 Antarctic circumpolar convergence zone under a reduced meridional temperature gradient has

171 been associated with a reduced sea-ice field[9], and the upwelling of warm, CO_2-rich

172 Circumpolar Deep Water (CDW)[14,23] onto the continental shelf with consequences for the

173 stability of marine grounding-lines[24]. The dominance of precession-paced variability and the

174 corresponding reduction in obliquity influence revealed by our data after ~3.3 Ma is

175   interpreted to reflect a declining influence of oceanic forcing on EAIS stability and extent, as

176   the southern high latitudes cooled. Both model and geological reconstructions imply that past

177   Antarctic ice sheet expansion is closely linked with development of the sea-ice field[25]

178   potentially resulting in northward migration of westerly winds and Southern Ocean fronts[9]. In

179   addition, sea ice expansion after 3.3 Ma likely restricted upwelling and ventilation of warm

180   CO_2 rich CDW at the Antarctic margin acting to further enhance climate cooling, which has

181   been linked in models to a change in the frequency of the orbital response of polar ice

182   sheets[26]. Under such a scenario, a warmer climate state during the Early to mid-Pliocene with

183   higher atmospheric CO_2 concentration[27] required less insolation to melt sea ice, thus

184   extending the austral melt season with its duration more strongly influenced by mean annual

185   insolation controlled by obliquity (Fig. 2d), rather than seasonal insolation intensity

186   controlled by precession[6]. Late Pliocene cooling raised the melt threshold such that the

187   duration of the melt season was restricted to times of austral summer insolation maxima

188   controlled by precession (Fig. 2c), with extensive sea-ice cover for much of the summer

189   season limiting the influence of CDW on marine grounding line instability. This supports the

190   notion that the length of the summer melt season is controlled by the overall climate state,

191   and is the primary influence on the frequency response of the EAIS to orbital forcing[7].

192   Our data also supports the general concept of precession-driven, antiphase oscillations

193   in inter hemispheric ice volume that may be cancelled out in globally integrated proxy

194   records between ~3.3-2.5 Ma (e.g. ref. 4). Furthermore, by using paleomagnetic reversals

195   from the bottom and top of the Kaena Subchron, to synchronise proxy reconstructions of

196   summer climate in Antarctica (U1361) and the Arctic (Lake El'gygytyn)[28], we demonstrate a

197   clear anti-phased response to precessional forcing on inter hemispheric climate (Fig. 3a;

198   Extended Data Table 2). However, the argument that the intensity of summer insolation was

199   a direct control on surface melt of a dynamic EAIS with a terrestrial ablation margin is not

supported by this study. The geometry of strata on the Wilkes Land continental shelf indicate

that the EAIS periodically expanded towards the continental shelf edge during glacial

maxima in the Pliocene[12] (Extended Data Fig. 1) and suggests most Antarctic ice volume

variance at this time was growth and retreat of the marine-based ice sheets. Indeed, iceberg

calving appears to be associated with sea-ice melt as evidenced by the covariance of IBRD

peaks with facies transitions going from relatively colder glacial maxima conditions to

warmer interglacial minima conditions as implied by open ocean primary productivity (opal)

in our data. This is particularly true for the Late Pliocene from 3.3 to 2.5 Ma, but during the

Early Pliocene, when the sea ice field was reduced and the ice sheet was in more direct

contact with oceanic influences, iceberg calving occurred more regularly within both glacial

and interglacial facies. Based on the significant decrease in IBRD after 2.5 Ma (Fig. 2; 3) and

Southern Ocean records inferring decreased SSTs[9,29] , we also infer the EAIS started to

stabilize and became less sensitive to ocean induced melting compared to the WAIS[24], with

fully-glaciated East Antarctic ice volume fluctuating by a similar magnitude to that of Late

Pleistocene glacial cycles (e.g. 15-20 m ice volume equivalent sea level)[8]. Notwithstanding

this relative stability, ~20-kyr-duration Antarctic ice volume fluctuations of this magnitude

could have offset a larger out-of-phase precessional change in Northern Hemisphere ice

volume (e.g. 20-40m), resulting in an enhanced obliquity signal in globally integrated proxy

records between 3.33 and 1.0 Ma[4]. Notwithstanding this, a range of proxy evidence including

ice rafted debris records[20] and a recent dust flux record[30] confirm that NH ice sheet variability

and climate primarily responded to obliquity. In contrast, our results imply that Southern

Ocean sea-ice feedbacks caused a fundamentally different response of the marine-based

sectors of the EAIS under a cooler Late Pliocene/Early Pleistocene climate state,

characterized by a dominance of precession-paced variability.

224   We conclude that prior to the development of Northern Hemisphere ice sheets at ~3.3

225   Ma, East Antarctic Ice Sheet variability responded primarily to obliquity and demonstrated

226   high sensitivity on orbital timescales to a relatively small increase in atmospheric CO_2

227   concentration and mean global surface temperature. With atmospheric CO_2 concentrations

228   and global surface temperatures projected to remain above 400 ppm and >+2°C beyond

229   2100[31], our results suggest that the marine margins of EAIS ice sheet as well as the marine-

230   based WAIS, will become increasingly susceptible to ocean-forced melting providing the

231   potential for widespread mass loss raising sea-level by meters over the coming centuries.

232

233   **Methodology**

234   20cc samples were treated with H2O2 to remove organic material and 2M NaOH to

235   remove biogenic opal for grain size analysis. The dry weights of the samples were measured

236   before and after opal removal to obtain an opal weight and terrigenous weight percent. The

237   covariance of the opal weights to the Ba/Al (a productivity indicator) from XRF scans of the

238   core indicates that the majority of opal dissolved was due to diatom productivity rather than

239   volcanic glass (Extended Data Figure 8). Opal percentages also correspond well to the

240   independently determined visual core descriptions using smear slide estimates of biogenic

241   opal content. Biogenic content was dissolved from the 250 µm to 2 mm fraction of coarse

242   sand used to indicate IBRD. The MAR of the coarse sand fraction was then estimated using

243   the following equation:

244

245   IBRD MAR = CS% * DBD * LSR

246

247   where IBRD MAR is the mass accumulation rate ($g/cm^2/k.y.$), CS% is the terrigenous coarse-

248   sand weight percent, DBD is the dry-bulk density of the nearest value (g/cm^3) and LSR is the

249   interval average linear sedimentation rate (cm/k.y.). Visual examination of every individual

250   sample for authigenic minerals and volcanic glass was conducted and these were absent,

251   indicating that the IBRD volume percent was directly equivalent to the terrigenous CS%[32].

252   The distribution of mm-scale silt and sand laminae (with rare cm-scale beds) was

253   collected using high-resolution line scan images of the split core face. The thickness and

254   stratigraphic depth of each laminae was accurately mapped through the use of a purpose built

255   image analysis script in Matlab©.

256   Using the age model of[11] we performed a basic spectrogram analysis script in

257   Matlab© followed by power spectral analysis using the Multi-Taper method (MTM)[33] with

258   five data tapers for the untuned IBRD MAR and biogenic opal time series at ~3 kyr

259   resolution. Equal time spacing was achieved by linear interpolation. Time series for power

260   spectra was broken into two segments as there is a gap in our data exceeding 100 kyrs that

261   predates 3.33 Ma. The statistical significance of spectral peaks was tested relative to the null

262   hypothesis of a robust red noise background, AR(1) modeling of median smoothing, at a

263   confidence level of 90% and 95%[34].

264

265   **Author Contributions**

266   MOP, RM, TN designed the study, conducted sedimentological and time series analyses and

267   wrote the paper. CE and HB led IODP Expedition 318 and provide seismic reflection data

268   interpretation. FJ and CE analysed XRF geochemical data. LT led development of the age

269   model. MR contributed to writing the manuscript. All authors contributed to the

270   interpretations.

271

272   ***Integrated Ocean Drilling Program Expedition 318 Scientists**

273   Klaus, A[1], Fehr, A[2], Bendle, J. A. P.[3], Bijl, P. K.[4] , Bohaty., S.M.[5], Carr, S. A.[6], Dunbar, R.

274   B.[7], Flores, J.A.[8], Gonzalez, J.J.[9], Hayden, T. G.[10], Iwai, M.[11], Katsuki, K.[12], Kong, G. S.[13],

275   Nakai, M.[14], Olney, M. P.[15], Passchier, S.[16], Pekar, S. F.[17], Pross, J.[18], Riesselman, C.R.[19],

276   Röhl, U.[20], Sakai, T.[21], Shrivastava, P. K.[22], Stickley, C. E.[23], Sugasaki, S.[24,25], Tuo, S.[26], van

277   de Flierdt, T.,[27] Welsh, K.[28] , Williams, T.,[29] & Yamane, M.[30]

278

279   [1]United States Implementing Organization, Integrated Ocean Drilling Program, Texas A&M

280   University, 1000 Discovery Drive, College Station, TX 77845, USA. [2]RWTH Aachen

281   University, Institute for Applied Geophysics and Geothermal Energy, Mathieustrasse 6, D-

282   52074 Aachen, Germany. [3]Geographical and Earth Sciences, University of Glasgow, Gregory

283   Building, Lilybank Gardens, G128QQ Glasgow, UK. [4]Department of Chemistry and

284   Geochemistry, Colorado School of Mines, 1500 Illinois Street, Golden, CO 80401, USA.

285   [5]Ocean and Earth Science, National Oceanography Centre Southampton, University of

286   Southampton, European Way, SO14 3ZH, Southampton, UK. [6]Department of Geological and

287   Environmental Sciences, Stanford University, 325 Braun Hall, Building 320, Stanford, CA

288   94305-2115, USA. [7]Department of Environmental Earth System Science, Stanford

289   University, 325 Braun Hall, Building 320, Stanford, CA 94305-2115, USA. [8]Department of

290   Geology, Universidad de Salamanca, 37008, Salamanca, Spain. [9]Instituto Andaluz de

291   Ciencias de la Tierra, CSIC-UGR, 18100 Armilla, Spain.[10]Department of Geology, Western

292   Michigan University, 1187 Rood Hall, 1903West Michigan Avenue, Kalamazoo, MI 49008,

293   USA. [11]Department of Natural Science, Kochi University, 2-5-1 Akebono-cho, Kochi 780-

294   8520, Japan. [12]Geological Research Division, Korea Institute of Geoscience and Mineral

295   Resources, 30 Gajeong-dong, Yuseong-gu, Daejeon 305-350, Republic of Korea. [13]Petroleum

296   and Marine Research Division, Korea Institute of Geoscience and Mineral Resources, 30

297   Gajeong-dong, Yuseong-gu, Daejeon 305-350, Republic of Korea. [14]Education Department,

298   Daito Bunka University, 1-9-1 Takashima-daira, Itabashi-ku, Tokyo 175-8571, Japan.

299   [15]Department of Geology, University of South Florida, Tampa, 4202 East Fowler Avenue,

300   SCA 528, Tampa, FL 33620, USA. [16]Earth and Environmental Studies, Montclair State

301   University, 252 Mallory Hall, 1 Normal Avenue, Montclair, New Jersey 07043, USA.

302   [17]School of Earth and Environmental Sciences, Queens College, 65-30 Kissena Boulevard,

303   Flushing, NY 11367, USA. [18]Paleoenvironmental Dynamics Group, Institute of Geosciences,

304   Goethe-University Frankfurt, Altenhöferallee 1, 60438 Frankfurt, Germany. [19]Departments of

305   Marine Science and Geology, University of Otago, PO Box 56, Dunedin 9054, New

306   Zealand.[20]MARUM – Center for Marine Environmental Sciences, University of Bremen,

307   Leobener Straße, 28359 Bremen, Germany. [21]Department of Geology, Utsunomiya

308   University, 350 Mine-Machi, Utsunomiya 321-8505, Japan. [22]Antarctica Division,

309   Geological Survey of India, NH5P, NIT, Faridabad 121001, Harlyana, India. [23]Department of

310   Geology, Universitet i Tromsø, N-9037 Tromsø, Norway. [24]Scripps Institution of

311   Oceanography, University of California, San Diego, La Jolla, California 92093-0220, USA,

312   [25]Department of Earth and Planetary Sciences, University of Tokyo, 7-3-1 Hongo, Bunkyo-

313   ku, Tokyo 113-0033, Japan. [26]School 223 of Ocean and Earth Science, Tongji University,

314   1239 Spring Road, Shanghai 200092, People's Republic of China. [27]Department of Earth

315   Science and Engineering, Imperial College London, South Kensington Campus, Prince

316   Consort Road, London SW7 2AZ, UK.[28]School of Earth Sciences, University of Queensland,

317   St Lucia, Brisbane QLD 4072, Australia. [29]Lamont Doherty Earth Observatory of Columbia

318   University, PO Box 1000, 61 Route 9W, Palisades, New York 10964, USA. [30]Earth and

319   Planetary Science, University of Tokyo, 7-3-1 Hongo, Bunkyo-ku, Tokyo 113-0033, Japan.

REFERENCES

321   1. Lisiecki, L. E. & Raymo, M. E. A Plio-Pleistocene stack of 57 globally distributed benthic

322    $\delta^{18}O$ records. *Paleoceanography* **20**, (2005).

323

324 2. Miller, K. G. et al. High tide of the warm Pliocene: Implications of global sea level for

325 Antarctic deglaciation. *Geology* **40**(5), 407-410 (2012).

326

327 3. Milanković, M. M. *Canon of Insolation and Ice Age problem*. Royal Serbian Academy

328 Special Publication (1941).

329

330 4. Raymo, M. E., Lisiecki, L. E., & Nisancioglu, K. H. Plio-Plesitocene ice volume, Antarctic

331 Climate, and the global δ^{18}O Record. *Science* **28**, 492-495 (2006).

332

333 5. Raymo, M. E., & Huybers, P. Unlocking the mysteries of the ice ages. *Nature* **451**, 284-

334 285 (2008).

335

336 6. Huybers, P., & Tziperman, E. Integrated summer insolation forcing and 40,000-year

337 glacial cycles: the perspective from an ice-sheet/energy-balance

338 model. *Paleoceanography* **23**(1), PA1208 (2008).

339

340 7. Naish, T. et al. Obliquity-paced Pliocene West Antarctic ice sheet oscillations. *Nature*

341 **458**(7236), 322-328 (2009).

342

343 8. Pollard, D. & DeConto, R. Modeling West Antarctic ice sheet growth and collapse through

344 the past five million years. *Nature* **458**, 329-332 (2009).

345 9. McKay, R. et al. Antarctic and Southern Ocean influences on late Pliocene global cooling.

346 *PNAS* **109**, 6423-6428 (2012).

347

348   10. Lucchi, R. G. et al. Mid-late Pleistocene glacimarine sedimentary processes of a high-

349   latitude, deep-sea sediment drift (Antarctic Peninsula Pacific margin). *Marine Geology* **189**,

350   343–370 (2002).

351

352   11. Tauxe, L. et al. Chronostratigraphic framework for the IODP Expedition 318 cores from

353   the Wilkes Land margin: constraints for paleoceanographic reconstruction.

354   *Paleoceanography* **27**, (2012).

355

356   12. Eittreim, S. L., Cooper, A. K. & Wannesson, J. Seismic stratigraphic evidence of ice-

357   sheet advances on the Wilkes Land margin of Antarctica. *Sedimentary Geology* **96**, 131–156

358   (1995).

359

360   13. Anderson, R. F. et al. Wind-driven upwelling in the Southern Ocean and the deglacial rise

361   in atmospheric CO2. *Science* **323**, 1443-1448 (2009).

362

363   14. Toggweiler, J. R., Russell, J. L., & Carson, S. R. Midlatitude westerlies, atmospheric

364   CO2, and climate change during the ice ages. *Paleoceanography* **21,** (2006).

365

366   15. Cook, C. P. et al. Dynamic behaviour of the East Antarctic Ice Sheet during the Pliocene

367   warmth. *Nature Geoscience* **6**, 765-769 (2013).

368

369   16. Depoorter, M. A. et al. Calving fluxes and basal melt rates of Antarctic ice

370   shelves. *Nature* (2013).

371

372   17. Mackintosh, A. et al. Retreat of the East Antarctic ice sheet during the last glacial

373   termination. *Nature Geoscience* **4**, 195-202 (2011).

374

375   18. Zachos, J et al., Climate Response to Orbital Forcing Across the Oligocene-Miocene

376   Boundary, *Science* **292**, 274-276 (2001).

377

378   19. Pälike, H. et al. The heartbeat of the Oligocene climate system. *Science* **314**(5807), 1894-

379   1898 (2006).

380

381   20. Kleiven, H.F., Jansen, E., Fronval, T. and Smith, T.M. Intensification of Northern

382   Hemisphere glaciations in the circum Atlantic region (3.5-2.4 Ma) - ice-rafted detritus

383   evidence. Palaeogeo. Palaeoclim. Palaeoecol. **184**(3-4), 213-223 (2002).

384

385   21. Williams, G. D., Bindoff, N. L., Marsland, S. J., & Rintoul, S. R. Formation and export of

386   dense shelf water from the Adélie Depression, East Antarctica. *J. Geophys. Res.* **113**, C04039

387   (2008).

388

389   22. Martínez-Garcia, A. et al. Southern Ocean dust-climate coupling over the past four

390   million years. *Nature* **476**, 312-315 (2011).

391

392   23. Martinson, D. G., Stammerjohn, S. E., Iannuzzi, R. A., Smith, R. C. & Vernet, M.

393   Western Antarctic Peninsula physical oceanography and spatio-temporal variability. *Deep

394   Sea Res. II* **55**, 1964–1987 (2008).

395

396   24. Pritchard, H. D. et al. Antarctic ice-sheet loss driven by basal melting of ice shelves.

397   *Nature* **484**, 502–505 (2012).

398

399   25. DeConto, R., Pollard, D., & Harwood, D. Sea ice feedback and Cenozoic evolution of

400   Antarctic climate and ice sheets. *Paleoceanography* **22** (3), (2007).

401

402   26. Huybers, P., & Denton, G. Antarctic temperature at orbital timescales controlled by local

403   summer duration. *Nature Geoscience* **1**, 787-792 (2008).

404

405   27. Seki, O. et al. Alkenone and boron-based Pliocene pCO2 records. *Earth Planet. Sci. Lett.*

406   **292,** 201-211 (2010).

407

408   28. Brigham-Grette, J. et al. Pliocene Warmth, Polar Amplification, and Stepped Pleistocene

409   Cooling Recorded in NE Arctic Russia. Science 340, 1421-1427 (2013).

410

411   29. Escutia, C. et al. Circum-Antarctic warming events between 4 and 3.5 Ma recorded in

412   marine sediments from the Prydz Bay (ODP Leg 188) and the Antarctic Peninsula (ODP Leg

413   178) margins. *Global & Planet. Change* **69**(3), 170-184 (2009).

414

415   30. Naafs, B. D. A. et al. Strengthening of North American dust sources during the late

416   Pliocene (2.7 Ma). *Earth & Planet. Sci. Lett.* **317**, 8-19 (2012).

417

418   31. IPCC, 2013: *Climate Change 2013: The Physical Science Basis. Contribution of Working*

419   *Group I to the Fifth Assessment Report of the Intergovernmental Panel on Climate Change*

420   [Stocker, T. F., D. Qin, G.-K. Plattner, M. Tignor, S. K. Allen, J. Boschung, A. Nauels, Y.

421 Xia, V. Bex and P. M. Midgley (eds.)]. Cambridge University Press, Cambridge, United
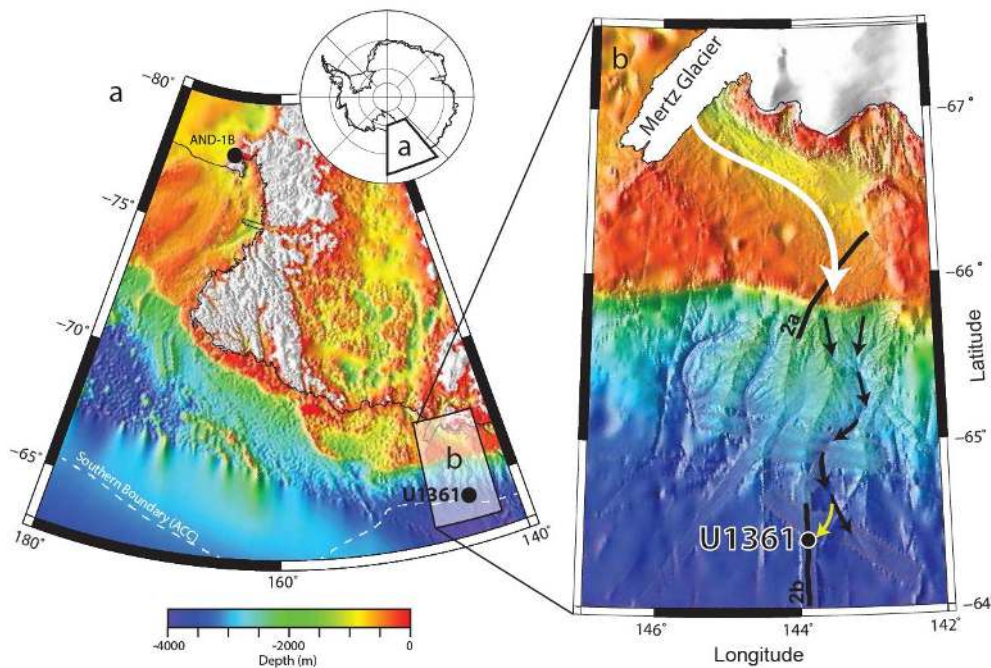
422 Kingdom and New York, NY, USA, **in press**.

423

424 ACKNOWLEDGEMENTS

431

432 FIGURE LEGENDS

433

434   Figure 1. **Location of Site U1361 and bathymetry offshore of the Wilkes Land margin,**

435   **Antarctica**. Also shown is the location of the Miocene-Plesitocene ANDRILL AND-1B core

436   recovered in the northwestern corner of the Ross Ice Shelf, the southern boundary of the

437   Antarctic Circumpolar Current (ACC), the Mertz Glacier tongue and paleo ice sheet drainage

438   path (white arrows) extending off shore into a slope and rise canyon system. Black lines

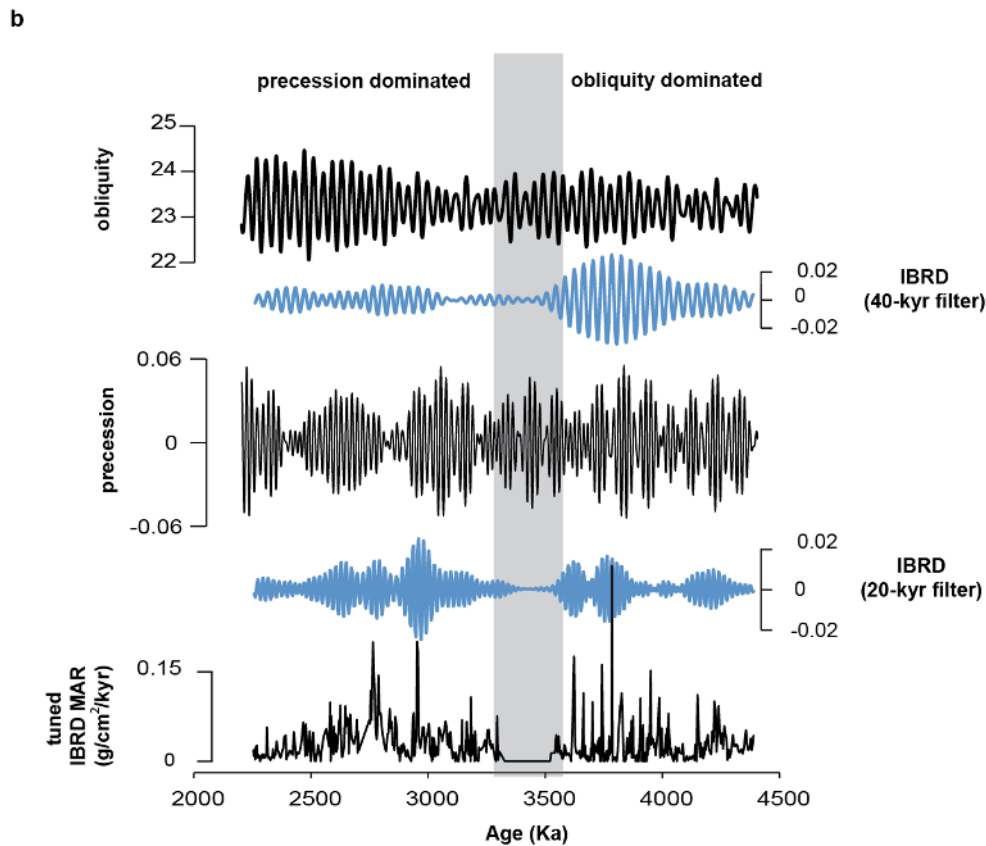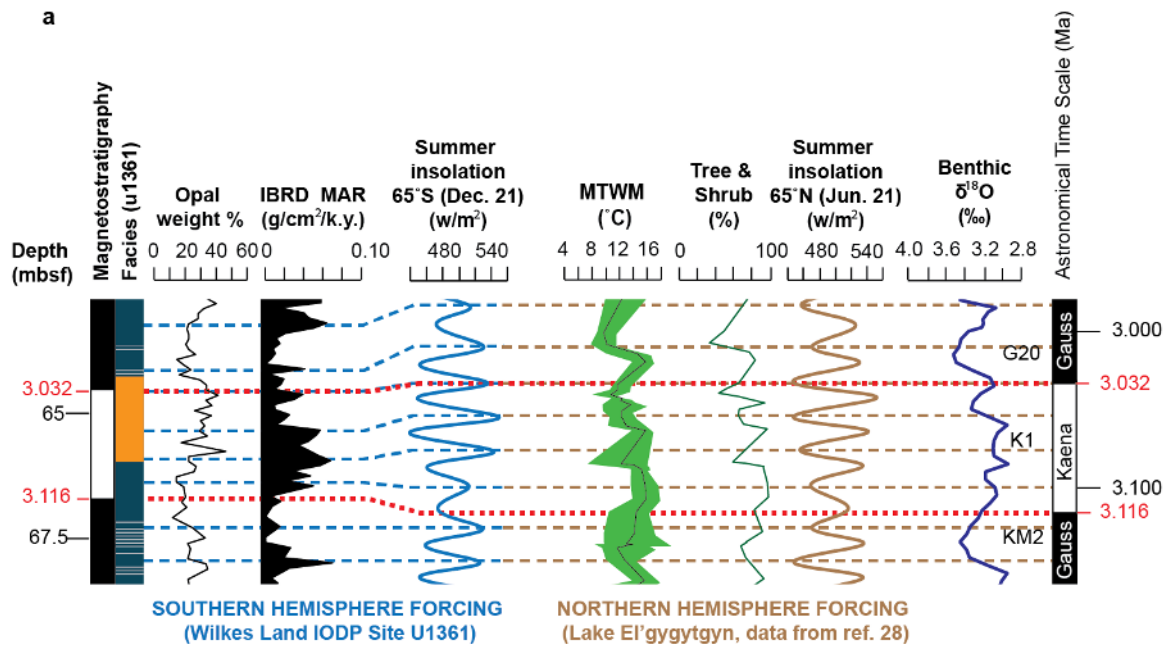439   represent seismic reflection profile tracks represented in Extended Data Figure 1.

440
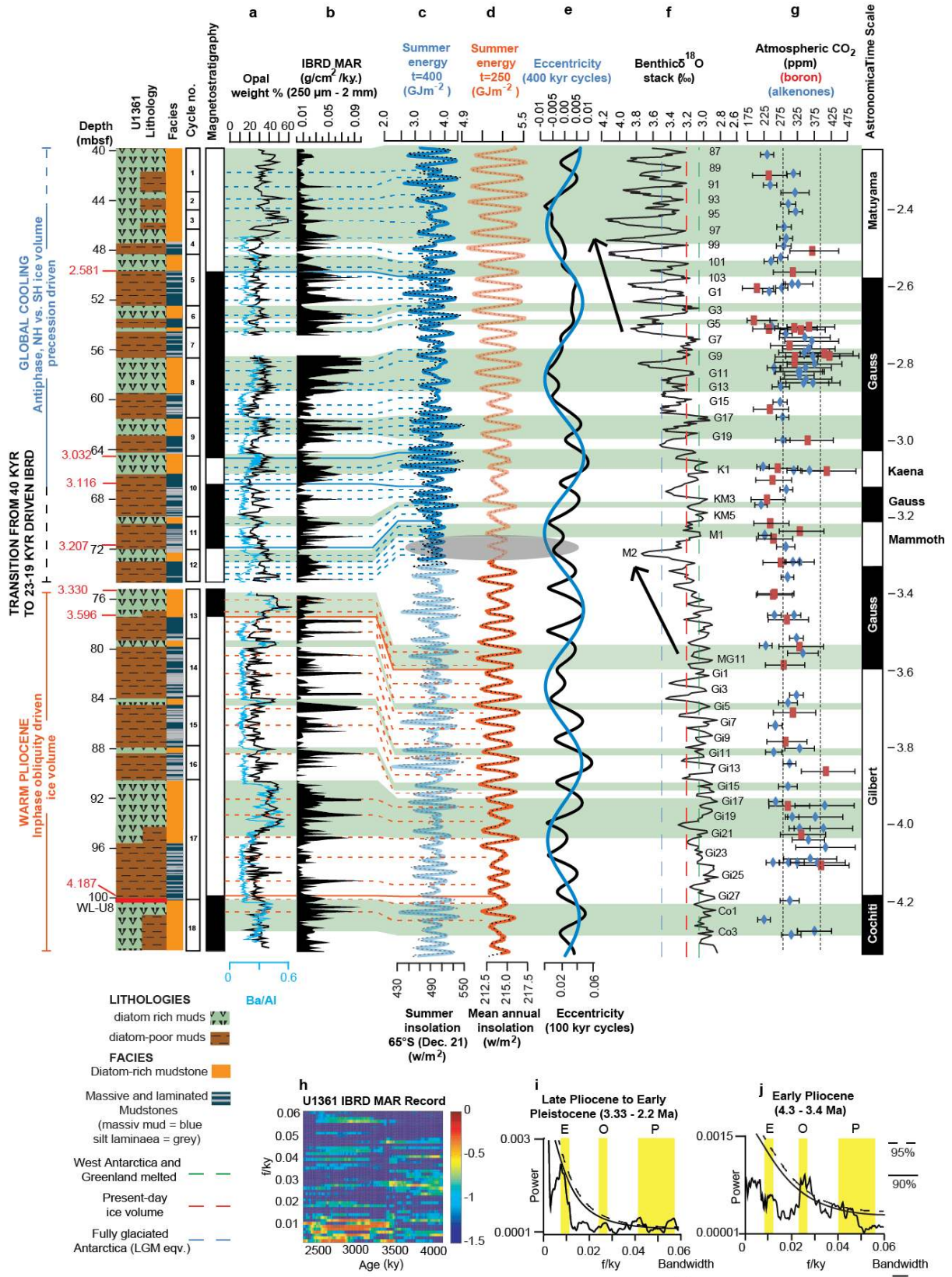
Figure 2. **Depth series developed for IODP site U1361 sediment core between 4.4-2.2Ma**

of (a) opal percent, (b) IBRD MAR correlated with time series of (c) January insolation

443   **and total integrated summer energy (where melt threshold [t]=400GJm^{-2}), (d) mean**

444   **annual insolation and   total integrated summer energy (where melt threshold**

445   **[t]=250GJm^{-2}), (e) eccentricity, and (f) the stacked benthic δ^{18}O record[1].** Also shown is

446   the down core distribution of lithofacies, lithological cycles and magnetic polarity

447   stratigraphy[20]. Maxima in productivity estimates of biogenic opal weight percent and Ba/Al

448   covary with bioturbated/diatom-rich mudstone facies. Grey shaded elipse denotes alignment

449   between a 1.2 Ma node in (d) obliquity modulated mean annual insolation and (e) a 400-kyr

450   minimum in eccentricity which favours polar ice sheet growth and corresponds to (f) a 1‰

451   glacial δ^{18}O excursion culminating with MIS M2 (arrow). A significant increase in (f) δ^{18}O

452   glacial values from 2.7 Ma (arrow) corresponds with a marked decline in the amplitude of (a)

453   IBRD and a 100ppm decrease in (g) reconstructed atmospheric CO_2 concentration[27]. An (h)

454   evolutive spectrogram of IBRD MAR time series and frequency spectra of (i) Late Pliocene

455   to Early Pleistocene (3.3-2.2Ma) and (j) Early Pliocene (4.3-3.4Ma) IBRD MAR time series

456   show transferral of spectral power from ~40-kyr frequency dominance prior to 3.3Ma to the

457   100-kyr and 23-19-kyr frequency bands after 3.3Ma.

458

a

SOUTHERN HEMISPHERE FORCING
(Wilkes Land IODP Site U1361)

NORTHERN HEMISPHERE FORCING
(Lake El'gygytgyn, data from ref. 28)

b

precession dominated   obliquity dominated

459

Figure 3. **(a) Corrleation between high-latitude Northern (Lake El' gygytgyn) and**

460

Southern Hemisphere (U1361) climate records synchronised by the Kaena Subchron

461

paleomagnetic reversals illustrates the influence of interhemispheric, anti-phased

462

precision forcing. (b) Tuned IBRD MAR time series for U1361 record with output from

463

464 **band-pass filters at precession (20kyr) as well as obliquity (40kyr) frequencies.** Grey

465 shading represents a time gap missing from the U1361 record followed by IBRD minima at

466 ~3.3Ma associated with a 1.2 Ma node in obliquity and 400-kyr eccentricity-modulated node

467 in precession.

468 **ONLINE METHODS SECTION**

469 *Iceberg Rafted Debris Mass Accumulation Rate calculation*

470   588 samples where processed for grain size and IBRD analysis (Extended Data Table

471 1). The 250 µm to 2 mm fraction of coarse sand was used to indicate IBRD, as has been used

472 in previous Arctic and Antarctic studies (e.g., ref. 32 and 35). The calculation of an Iceberg

473 Rafted Debris Mass Accumulation Rate (IBRD MAR) followed the methodology used by[32].

474 As recommended for samples with a mixed biogenic and terrigenous component in that

475 methodology, the >250 µm fraction was dissolved of biogenic silica using 2M NaOH. After

476 biogenic content was dissolved samples were then dry sieved at 150 and 250 µm to 2 mm

477 grain size. Each sample was then examined again under binocular microscope for volcanic

478 ash layers as well as any authigenic minerals, which were absent in all but one sample and

479 was excluded. The MAR of the coarse sand fraction was then estimated using the following

480 equation: IBRD MAR = CS% * DBD * LSR,

481

482 where IBRD MAR is the mass accumulation rate ($g/cm^2/k.y.$), CS% is the coarse-sand weight

483 percent, DBD is the dry-bulk density of the nearest value (g/cm^3) and LSR is the interval

484 average linear sedimentation rate (cm/k.y.). The relative abundance of IBRD in the %CS

485 fraction (c.f. ref. 32) was determined the visual examination of every individual sample for

486 authigenic minerals and volcanic ashes, and dissolution of the biogenic component, thus

487 resulting in the CS% being composed entirely of IBRD.

488

489   *Grain size distribution of the fine-grained (<150 um) material*

490   The fine-grained fraction was recovered by wet sieving at 150 µm followed by the

491   removal of organic material using 30% H_2O_2 and biogenic opal using 2M NaOH. Sampled

492   intervals were analysed for grainsize fractions using a LS 13 320 Laser Diffraction Particle

493   Size Analyzer, using the settings as defined by[36], to correct for the analytical overestimation

494   of the clay fraction (<4 µm). The percent medium-sand fraction (150 to 250 µm) was

495   obtained following wet sieving at 150 µm and dry sieving at 250 µm with biogenic

496   components removed. Biogenic opal weight percent was obtained from dried weights before

497   and after NaOH dissolution during the grain size processing (Extended Data Table 1). This

498   method of opal wt% data carries a degree of analytical uncertainty, as the alkali treatment

499   may also leach clay minerals and volcanic glass. However, comparison to the facies (based

500   on smear slides) and to low-resolution quantitative opal data[15] show identical G/I cyclicity,

501   albeit with an overestimation (10-20%). There is also strong covariance between the opal

502   wt% and the Ba/Al, with any scatter or outliers potentially due to some of opal being the

503   component of the turbidites (some of the silt laminae were diatom-rich[37]) rather than a pure

504   pelagic component.

505

506   *Identification of iceberg rafted debris versus lag deposits*

507   In order to make the distinction between enrichments in the CS% due to current

508   winnowing of the fine fraction, we determined the sorting parameter[38] of fine grain

509   terrigenous sediment (i.e., biogenic component removed), following the methodology of

510   previous studies recovered from sediment drifts on the continental rise around the Antarctic

511   margin (Extended Data Fig. 4)[39]. IBRD peaks coinciding with well-sorted terrigenous

512   material are likely to be a concentration of coarse material following winnowing of fine-

513   grained sediments by higher energy bottom currents. Whereas, IBRD peaks correlating with

514 poorly to very-poorly sorted material reflect actual IBRD events superimposed onto the

515 background hemipelagic sedimentation. Furthermore, peaks of well-sorted terrigenous

516 material also serve to identify potential hiatuses between the chronostratigraphic tiepoints

517 (i.e., magnetic reversals) in our record related to current winnowing[39]. There is a complete

518 absence of well-sorted material in all samples anaylsed, further supporting our assumption of

519 no major hiatuses in the studied interval. All IBRD peaks coincide with poorly to very-poorly

520 sorted sediment, indicating IBRD events are not the product of lag deposits and the lack of

521 moderately- to well-sorted terrigenous sediment indicates bottom current energy was never

522 high enough energy for erosion to dominate over deposition. Along-slope currents are also

523 unlikely to have a major erosive control, with modern-day bottom currents flowing eastward

524 across the drill site at a velocity of 1.8-6.6 cms^{-1} [40], which is well-below the current strength

525 required for the onset of selective deposition (10-12cms^{-1}) or extensive winnowing of the fine

526 fraction (>20$cm\ s^{-1}$)[41]. Downslope currents, resulting from High Salinity Shelf Water masses

527 passing down the continental rise, are also low-energy throughout the Plio-Pleistocene in

528 these distal levee environments along the Wilkes Land margin[42,43].

529

530 ***Iceberg Rafted Debris as proxy***

531   As the Antarctic ice sheets lose 50-80% of their mass from iceberg calving[16],

532 significant changes in the mass balance of marine-based ice sheet should be evident in high-

533 quality IBRD records, provided certain caveats are considered.

534

535   We have demonstrated that the untuned IBRD contains a statistically significant

536 signal at orbital periodicities throughout the record (Fig. 2), therefore, suggesting iceberg

537 calving is not a random process at this scale. Orbital pacing has also been qualitatively

538 implied by previous studies along the EAIS margin, but these studies did not statistically

539 identify the frequencies of that pacing as well as the variance between the 40-kyr and 20-kyr

540 cycles[29,39]. While late Pleistocene studies of Antarctic sediment cores display a glacial to

541 interglacial cyclicity, with peaks in IBRD occurring during deglaciation and interglacials,

542 these records can reflect distinct regional differences in ice sheet response to glacial-

543 interglacial processes, including bottom current winnowing and changes in sedimentation

544 rates (e.g., ref. 44). We have assessed the influence both of these processes in U1361 in the

545 main text as well as above, and we are confident that they are not a major influence on the

546 IBRD record.

547

548   Another important consideration is that Antarctica's larger ice shelves lack basal

549 debris (i.e., Ross Ice Shelf), which melts out close to the grounding line, and consequently

550 does not distribute abundant amounts of ice rafted debris to the ocean. However, smaller ice

551 shelves and ice tongues source sediment-laden icebergs containing significant basal debris

552 layers[45]. Thus, we interpret the U1361 record to reflect IBRD from the calving of sediment-

553 laden bergs from outlet glaciers draining the EAIS (either the Ross Sea or Wilkes Land

554 margin). However, we stress this does not exclude the presence of local ice shelves which

555 may have played an important role in buttressing the grounded ice sheet, particularly during

556 glacial periods. Thus, if there was a signficant ice shelf contribution to our record (i.e., low

557 IBRD = fringing ice shelves; high IBRD = non fringing ice shelves), then this is directly

558 relevant to assessing changes in dynamical ice discharge. Also, large ice shelves (such as the

559 Ross Ice Shelf) may not have persisted through glacial minima in the Pliocene (e.g., the

560 AND-1B record[7,8]). Thus, an alternative explanation for the decrease in IBRD MAR after 2.5

561 Ma, or during nodes in precession and obliquity, may reflect increased persistence or duration

562 of large fringing ice shelf shelves (and thus "cleaner" icebergs) during these colder intervals,

563 which in turn would have restricted dynamical ice discharge.

564

565   Changes in surface ocean currents are unlikely to have influenced iceberg drift

566 patterns at U1361. The dominant easterly flow over the site (Antarctic Coastal Current and its

567 associated front - Antarctic Slope Front) is unlikely to have changed direction, due to

568 bathymetric (i.e., the continental rise/shelf break) and geostrophic considerations, as

569 demonstrated under the scenarios of a greatly reduced EAIS[25]. IBRD peaks from further in

570 the Southern Ocean (e.g., polar front) may represent glacial maxima as icebergs can survive

571 for longer time periods in the colder glacial period waters. However, U1361 is proximal

572 enough to outlet glaciers of the Antarctic margin for smaller "dirty" icebergs derived from

573 these sources to survive moderate levels of SST warming (as inferred for the Pliocene), but

574 not so close as to be influenced by a single outlet glacier, or a single iceberg dumping[46]. The

575 3500m water depth and open ocean location of U1361 (with only seasonal winter sea) means

576 icebergs would never be "locked in" place over the drill site, and would pass over the drill

577 site very rapidly (i.e., minutes as they do today).

578

579 ***XRF Ba/Al analysis***

580   The bulk major element composition was measured between cores U1361A-6H to

581 11H using an Aavatech TMX-ray fluorescence (XRF-Scanner) core scanner at the IODP-

582 Core Respository/ Texas A&M University laboratories (USA). Non-destructive XRF core-

583 scanning measurements were performed at 10 kV in order to measure the relative content of

584 elements ranging from aluminum (Al) to barium (Ba). Measurements were acquired every

585 5cm. In addition, discrete samples were taken to measure Ba and Al by X-Ray Fluorescence

586 (XRF) using pressed pellets prepared by pressing about 5 g of ground bulk sediment into a

587 briquet with boric acid backing. The quality of the analysis was monitored with reference

588 materials showing high precision with 1 sigma 1.0e3.4% on 16 data-sets at the 95%

589   confidence level. For XRF 42 samples were selected in a 20 m representative interval (47 to

590   67 mbsf) at ~40-60 cm intervals. Compared Ba and Al trends using both techniques are

591   virtually identical and indicate that obtained XRF-Scanner data are robust and reliable.

592

593   *Age Model*

594   The age model for the U1361 record was developed by an integration of

595   biostratigraphic datums (diatom, radiolarian, calcareous nannofossils and dinoflagellate cyst)

596   and a magnetic polarity zonation[11]. We used the biostratigraphically-constrained

597   magnetostratigraphic tie points for correlations between the IBRD MAR record presented in

598   this study and orbital paramters as well as the benthic $\delta^{18}O$ stack[1]. The age model of U1361

599   highlights the continuous nature of the Plio-Pleistocene interval in the U1361 record

600   (Extended Data Fig. 5) with long-term sedimentation rates estimated at ~30 m/m.y., with no

601   major time gaps due to erosion. However, a single condensed interval is identified around 3.3

602   Ma (~74.52 mbsf) (Fig. 2; Extended Data Fig. 5). The Early Pliocene from ~4.2 Ma to Early

603   Pleistocene at ~2.0 Ma contains no major core disturbances with only one major core gap

604   extending between ~3.6 to ~3.33 Ma[37]. The continuous and uniform nature of the Plio-

605   Pleistocene sedimentation rates in U1361, combined with the detailed grain size anaylses

606   discussed above indicates that winnowing is not a major influence on sedimentation at this

607   site.

608

609   *Frequency Analysis*

610   Using the age model[11] we performed evolutionary spectral analysis in Matlab© (using

611   a spectrogram function developed by Peter Huybers and available at his website

612   http://www.people.fas.harvard.edu/~phuybers/Mfiles/index.html). This was followed by

613   power spectral analysis using the SSA-MTM toolkit for the Multi-Taper method (MTM)

614 analysis[33] with five data tapers for the untuned IBRD MAR (Fig. 2; Extended Data Fig. 6)

615 and biogenic opal weight percent (Extended Data Fig. 7) time series at 3 kyr resolution for

616 the Early Pliocene and 4 kyr resolution for the Late Pliocene-Early Pleistocene. Equal time

617 spacing was achieved by linear interpolation based on average temporal sample spacing of

618 time series segments as there is a gap in our data exceeding 100 kyrs that predates 3.33 Ma.

619 The statistical significance of spectral peaks was tested relative to the null hypothesis of a

620 robust red noise background, AR(1) modelling of median smoothing, at a confidence level of

621 90% and 95%[34]. Raw (AR1) models with a harmonic reshape set to a 90% threshold were

622 used to test the comparative variance in obliquity versus precession (Extended Data Fig. 6).

623   Tuning of the IBRD MAR record and bandpass filtering was conducted in

624 Analyseries[47] and filters for obliquity (central frequency of 0.025, bandwidth of 0.003) and

625 precession (central frequency of 0.045, bandwidth of 0.005) applied (Fig. 3b). Following

626 tuning, power spectra was carried out using the same parameters with the SSA-MTM toolkit

627 as the untuned data (Extended Data Fig. 7).

628

629 **SUPPLEMENTARY INFORMATION**

630 *Sedimentology Discussion*

631 ***Lithofacies***

632   Grain size data collected on Pliocene and Early Pleistocene intervals of U1361

633 confirm the lithofacies descriptions conducted by the shipboard scientific party[37] (Extended

634 Data Fig. 2, 3). The bioturbated Diatom-Rich/Bearing Mudstone (Extended Data Fig. 2 and

635 3a-b) is a light greenish grey silty clay with >25% diatoms in smear slides from lithological

636 descriptions, and > 25 wt% biogenic opal via NaOH dissolution. IBRD is common

637 throughout and values of Ba/Al, a productivity indicator[48], are high throughout and correlate

638   well with biogenic opal weight percents (Extended Data Fig. 8). This facies is directly

639   equivalent to Facies D in the initial reports volume of Exp. 318 Site U1361[37].

640

641   The Massive and Laminated Mudstone (Extended Data Fig. 3c-d) is olive grey and

642   massive in structure but contains packages of mm- to cm-scale silt and fine sand laminations,

643   variable bioturbation and mm-size silt lenses. Silt laminae/beds are internally massive,

644   contain sharp bases with a range from 1.3 mm to 2.5 cm in thickness with the mean thickness

645   4.5 mm, and laminae exceeding 1 cm in thickness (i.e. beds) are rare (<5% of all silt

646   laminae/beds). Diatom content is relatively poor throughout (<25 wt% biogenic opal) while

647   IBRD is common throughout.

648

649   *Facies interpretation*

650   The facies assemblages in the Pliocene-Early Pleistocene interval of U1361 are

651   consistent with existing facies models of sedimentation in distal channel-levee systems on the

652   lower continental rise from other regions globally[49] and from the Antarctic

653   margin[10,43,50,51,52,53]. The presence of normally graded well-sorted mm-scale silt laminae and

654   lenses in otherwise massive mudstones with sharp bases, but no internal structures or IBRD is

655   consistent with deposition by non-erosive spill-over of low density turbidite deposits onto a

656   channel levee in a distal lower continental rise setting (e.g. Ref. 10, 43, and 56). The laminae

657   themselves lack IBRD and bioturbation indicating relatively rapid deposition. Thus, the

658   characteristics of these laminae argue against a traction current (i.e. winnowing) origin of

659   deposition[10,43,56]. We also note the relationship between these laminae intervals of mudstones

660   are identical in nature to the mud turbidite facies (Extended Data Fig. 3c) "T3" to "T7"

661   beds[57], representing base-cut-out sequences and deposition in a low-density turbidity current

662   by overflow on the distal levee setting – i.e. a non-erosional depositional setting compared to

663   more proximal settings[43,56]. The presence of IBRD and bioturbation within intervals of the

664   massive mudstone facies, suggests that turbidite intervals where deposited by numerous

665   events over a relatively prolonged period, rather than a singular event.

666

667   A lull or reduction in persistent turbidity current activity is represented by the

668   presence of the bioturbated diatom-rich/bearing mudstone, consistent with the

669   Pelagite/Hemipelagite "F" beds[56]. Grain size analyses reveal that the bioturbated Diatom-

670   Rich/Bearing Mudstone facies are coarser (i.e., silty clays) than the massive mudstone

671   intervals (distinct silt laminae were excluded from this analysis) (Extended Data Fig. 2 and

672   3). The coarse nature of the bioturbated diatom rich/bearing facies deposits implies reworking

673   of older turbidites[41] (i.e. silt laminae and clays) and homogenization to a silty clay texture as

674   a result of bioturbation and bottom current processes between sediment gravity flow events.

675   The lack of erosional surfaces or coarse sands/gravel layers (i.e. lag surfaces) suggests that

676   although low-energy bottom currents or bioturbation acted to remobilize fine-grained

677   sediment, depositional processes dominated over erosional events.

678

679   However, in the Early Pleistocene (e.g., above 48 mbsf) bioturbation of diatom-rich

680   mudstones are distinguished by an overall decrease in IBRD, and an increase in overall silt

681   abundance displaying a gradual coarsening upwards (i.e. reverse grading) at the m-scale

682   (Extended Data Fig. 2c) and slight decrease in the long-term sedimentation rate (~2.33

683   cm/k.y.) compared with the Pliocene section (~3.10 cm/k.y.). Silt laminae become notably

684   rarer and less laterally continuous above 47.57 mbsf (Fig. 2), with only 57 laminae recorded

685   between 47.57 and 0 mbsf compared to 278 between 100 and 47.57 mbsf. Although distinct

686   continuous laminae are lacking, silt lenses and silt mottles are common and often display an

687   irregular alignment (Extended Data Fig. 2a). Combined, the textural characteristics, reverse

688 grading, and the sedimentary structures are consistent with silty-sandy contourite facies or,

689 more specifically for site U1361, bottom-current reworking[56] [Fig. 9]. In areas influenced by

690 active polynyas, bottom-current influenced sediments are highly bioturbated with irregularly

691 aligned silt lenses and mottles in which boundaries between different sediment layers become

692 difficult to distinguish[55]. This is interpreted to be consequence of the low-energy downslope

693 delivery of highly oxygenated and nutrient rich waters formed off the margin within active

694 polynya systems resulting in sediments containing high biogenic content and benthic activity.

695 In contrast, other regions in Antarctica not influenced by an active polynya system are

696 charactersied by anoxic conditions result in bottom-current influenced sediments of

697 hemipelagic grey muds with well-defined laminae that are rhythmic in nature, continuous,

698 lack bioturbation, contain low biogenic content, and contain sparse IRD or pebbly layers[43,55].

699 Thus, we have interpreted the reverse grading above ~48 mbsf, sparse IBRD, highly

700 bioturbated sediment with irregular alignment of silt lenses and mottles as representing colder

701 glacial conditions (in which events of sediment-laden iceberg discharge become rare) with

702 downslope currents due to enhanced polynya mixing off the Wilkes Land margin increases

703 the delivery of oxygenated nutrient rich water to the lower continental rise, increasing both

704 bioturbation and bottom current strength[43,55].

705

706   Seismic stratigraphic interpretation of existing multichannel reflection seismic

707 profiles crossing Site U1361 (Extended Data Fig. 1) provide further evidence that the

708 dominant sedimentary processes building these more distal levees is the fine-grained

709 components of turbidity flows traveling through the channel (where erosion does occur) and

710 from inter- and over-flow depositing sediment as hemipelagic drapes. Although, sediment

711 waves are observed locally in seismic lines from the lower rise that are perpendicular to the

712 margin (downslope processes), these are within the overbank deposits and are smooth (i.e.,

713   very low-relief) indicating that bottom-currents are not a dominant process at this distal site.

714   In contrast, sediment waves are very well-developed in older sequences (i.e., phase 2 of ref.

715   56), of upper Oligocene-Miocence age[37] in the lower continental rise and in more proximal

716   continental rise areas (i.e., where Site U1359 is located) suggesting a mixed turbidite and

717   bottom-current deposition[56,57,58]. It is during this time that the large levees and ridges form on

718   the Wilkes Land continental margin[37]. The change from sedimentation dominated by mixed

719   turbidite and bottom-current deposition (Phase 2) to sedimentation dominated by turbidite &

720   hemipelagic deposition (section containing sediments considered in this study) coincides with

721   a shift in sedimentary depocenters from the continental rise to the continental shelf[57]. Instead

722   of large levee deposits, low-relief overbank deposits spilling from the channels are commonly

723   observed on-lapping the previous levees and ridges[56,57].

724

725   ***Identification of glacial to interglacial sedimentation processes***

726   We interpret the massive/laminated mudstone facies as being predominately deposited

727   during periods of glacial maxima, with large volumes of unconsolidated sediment being

728   delivered to the continental shelf edge either through the deposition of till deltas or via

729   bedload rich turbid glacial melt water plumes during grounding line advance[10,12,42,59,61] with

730   turbidity current initiation due to slope failures on oversteepened foreset strata. This

731   interpretation is supported by seismic profiles that indicate glacial advances occurred

732   regularly since the Early Pliocene, as evinced by the onset of steeply dipping foresets and the

733   development of the modern progradational wedge above seismic unconformity WL-U8 which

734   can be traced from the continental shelf to rise and dated at 4.2 Ma (~100 mbsf) in

735   U1361[11,12,42] (Extended Data Fig. 1). Steeply dipping foresets are commonly found around

736   the margin of the Antarctic and are interpreted as being deposited in a proglacial setting at the

737   grounding line of ice streams, and are therefore a direct result of glacial advances to the shelf

738   edge [12,45,61,62].

739

740   We interprete the Diatom-Rich/Bearing Mudstone facies with IBRD and pervasive

741   bioturbation throughout to be predominately deposited during glacial minima. This

742   interpretation is supported by a recent isotopic Nd and Sr provenance study of the fine-

743   grained fraction in the Pliocene interval of the U1361 core and indicate that the eroding

744   margin of the EAIS had receded up to several 100 km inland[15]. The interplay of bioturbation

745   and downslope along slope currents results in an overall increase in the silt component, most

746   likely due to homogenization of sediment texture and removal of primary sedimentary

747   structures (i.e., silt laminae) within these intervals. Turbidity currents may have still been

748   delivering sediment during these intervals, perhaps as the consequence of isostatic

749   adjustments during postglacial retreats[42] or initiated by hypersaline density flows of high

750   salinity shelf waters passing down the continental rise. However, the homogenization of these

751   sediments suggests that turbidity current activity may have been less frequent. Reduced

752   turbidity current activity does not explain these facies alone, as changes in biogenic opal

753   weight percent covary with Ba/Al measurements within these diatom-rich/bearing intervals

754   (Extended Data Fig. 8). Thus, we interpret these intervals as representing times of enhanced

755   biogenic activity in the surface waters above the drill site, accompanied by a reduction in

756   turbidity current activity. We also note that during the Holocene, most fine grained sediment

757   is advected towards the inner continental shelf in the Mertz-Ninnis tough rather than towards

758   the shelf edge[63], due to the reverse slope morphology of the continental shelf that developed

759   in the Early Pliocene (i.e., above WL-U8), and thus it is likely this was also situation for Late

760   Pliocene-Pleistocene glacial minima[12].

761

762   The modern day position of the Southern Boundary of the ACC is ~10 km to the north

763   of Site U1361[64], and is the location of the Antarctic Divergence where relatively warm

764   UCDW upwells and biological productivity is high. Sea surface temperatures (SST)

765   reconstructions indicate that the Southern Ocean was up to +4°C warmer[65] with a

766   significantly reduced sea ice field during the warmest Pliocene in the Ross Sea[9], Prydz

767   Bay[29],[66] and Antarctic Peninsula[66] regions. For interglacial times, connections have been

768   made between southward zonal shifts in the intensity or location of southern westerlies and

769   their influence on incursions of CDW or modified CDW (MCDW) (when some mixing with

770   Antarctic waters has occurred) onto the continental shelves around Antarctica, with

771   consequences for the melting of the marine margins of the ice sheets[7,9,13,14,24,68]. However, the

772   main dynamical barrier for CDW (or MCDW) in Wilkes Land is the Antarctic Slope Front (at

773   the shelf break/upper continental rise), which creates a "V-shaped" isopycnial that extends

774   into intermediate water depths and restricts CDW incursions onto the continental shelf. Thus,

775   changes in the location, intensity or vigour of this current, related to the strength or location

776   of the zonal polar winds (i.e., polar easterlies and the subpolar westerlies), directly regulates

777   MCDW incursion, more so than a direct bathymetric control[21].
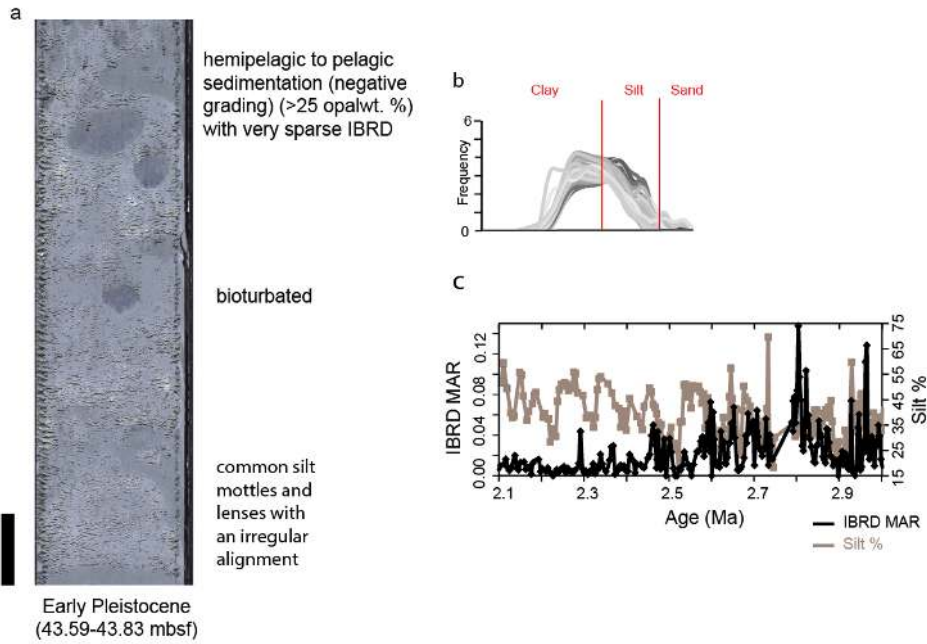
778

779   Early Pleistocene diatom-rich/bearing muds above ~48 mbsf, while displaying

780   similarities to Pliocene intervals, are distinctively different in IBRD content, arrangement in

781   silt lenses and mottles as well as displaying an apparent overall negative grading. The Early

782   Pleistocene intervals reflect reworking by downslope bottom currents in which enhanced

783   delivery of oxygenated and nutrient-rich waters formed in the Mertz Polynya promoting

784   productivity and bioturbation. Silt lenses and mottles appear more irregularly aligned

785   suggesting more vigourous bottom current remobilization of fine grain clay sediments, but

786   the lack of significant winnowing indicates these currents were still low energy. Sparse IBRD

787 suggests lulls in iceberg calving as disintegration events become less frequent as the ice sheet

788 stabilized and begins to fluctuate at the same extent as the Late Pleistocene glacial cycles.

789 These bottom currents appear to be related to low-energy downslope (rather than alongslope

790 currents), on account of the seismic data and modern oceanographic current data discussed

791 earlier. Continental rise channels (like the Jussieu channel) act as conduits for the delivery of

792 cascading high-salinity shelf water to the rise, however, these currents are low-energy and

793 appear non-erosived in this distal low-relief levee setting[43,69].

794

795
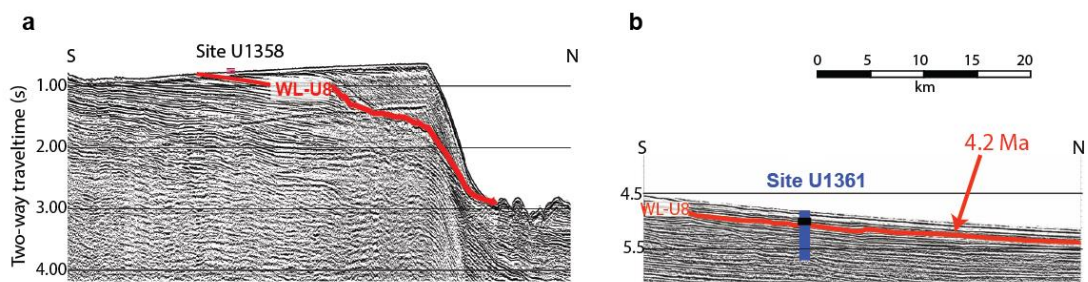
796

797 **Extended Data Figure 1. Seismic reflection profiles of Wilkes Land continental shelf**

798 **and Rise**. Interpreted seismic unconformity WL-U8 is highlighted in red extending from the

799 continental shelf (a) to the rise (b) with Site U1361 identified in blue. WL-U8 is age dated to

800 4.2 Ma[11,57].

Diatom Rich/Bearing Mudstone (Pleistocene)

a

hemipelagic to pelagic sedimentation (negative grading) (>25 opalwt. %) with very sparse IBRD

bioturbated

common silt mottles and lenses with an irregular alignment

Early Pleistocene (43.59-43.83 mbsf)

b

c

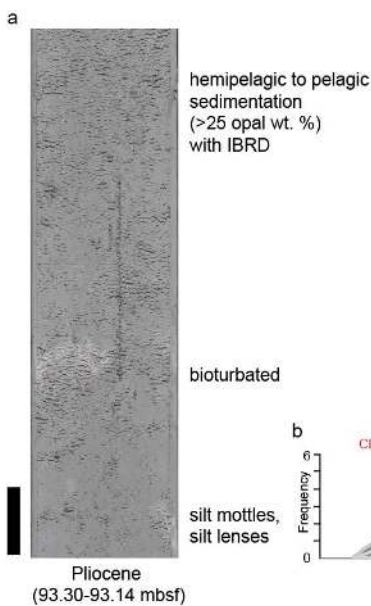**Extended Data Figure 2. (a) Representative photo highlighting distinct sediment characteristics of Early Pleistocene Diatom Rich/Bearing Mudstone lithofacies.** Black scale bar represents 3 cm. (b) Grain size frequencies of representative samples are displayed. (c) Draw down in Early Pleistocene IBRD coinciding with an overall increase in silt content.

Diatom Rich/Bearing Mudstone (Pliocene)

a

hemipelagic to pelagic sedimentation (>25 opal wt. %) with IBRD

bioturbated

silt mottles, silt lenses

Pliocene (93.30-93.14 mbsf)

b

Massive and Laminated Mudstone

c

bioturbated

wispy silt laminae

indistinct silt laminae

regular parrell mm silt laminae

sharp base

Pliocene (85.85-85.66 mbsf)

d
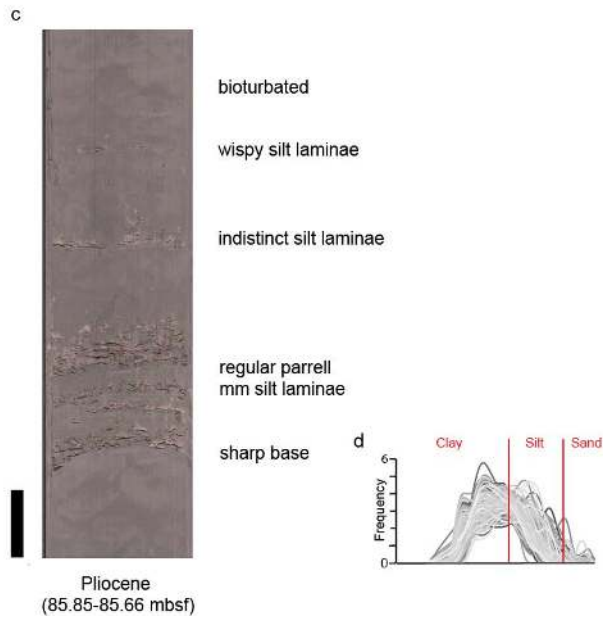
809 **Extended Data Figure 3. (a) Representative photo with (b) grain size frequencies**

810 **highlighting distinct sediment characteristics of Pliocene Diatom Rich/Bearing**

811 **Mudstone and (c-d) the Massive and Laminated Mudstone lithofacies.** Black scale bar
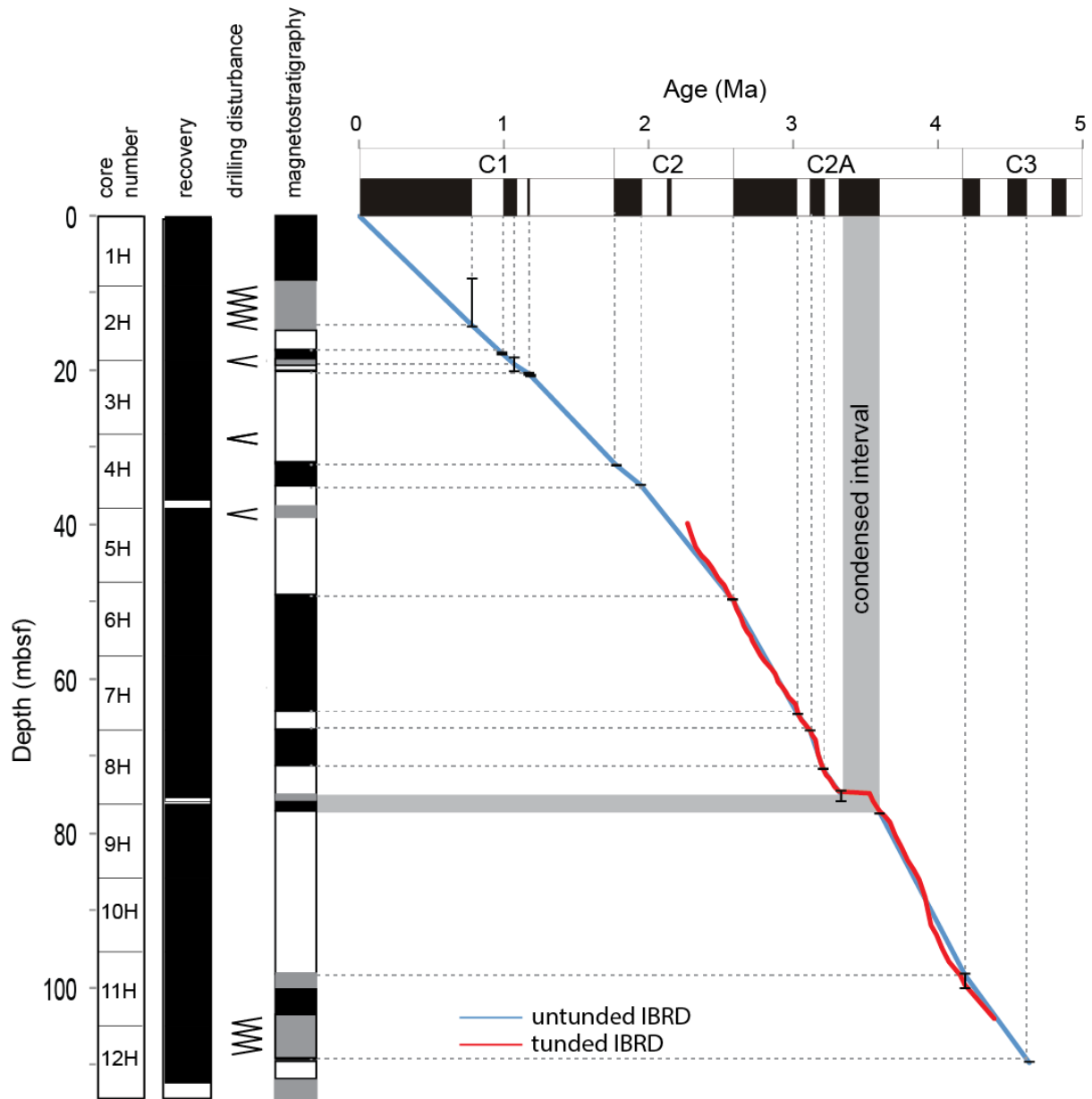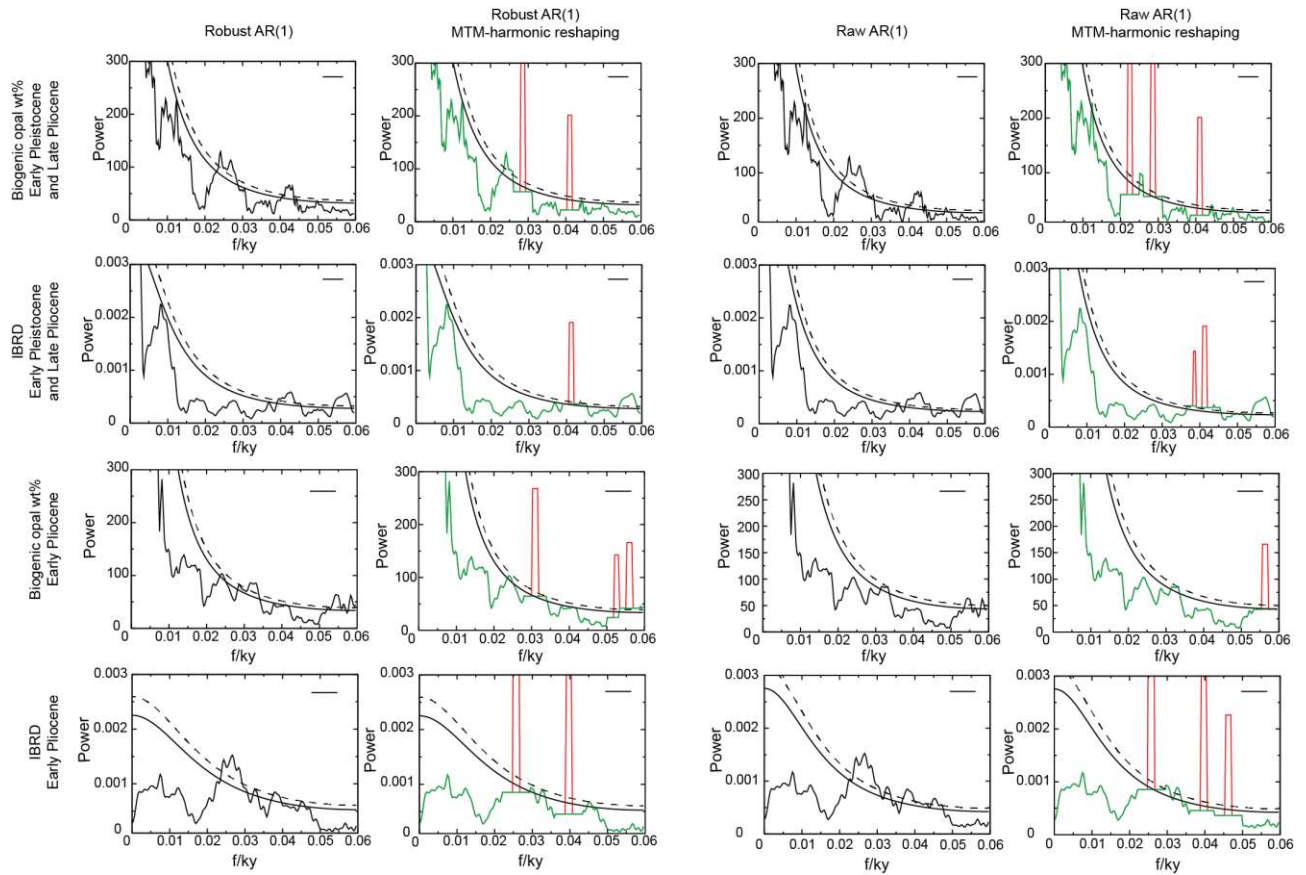
812 represents 3 cm.

813

814

815

816

820

825

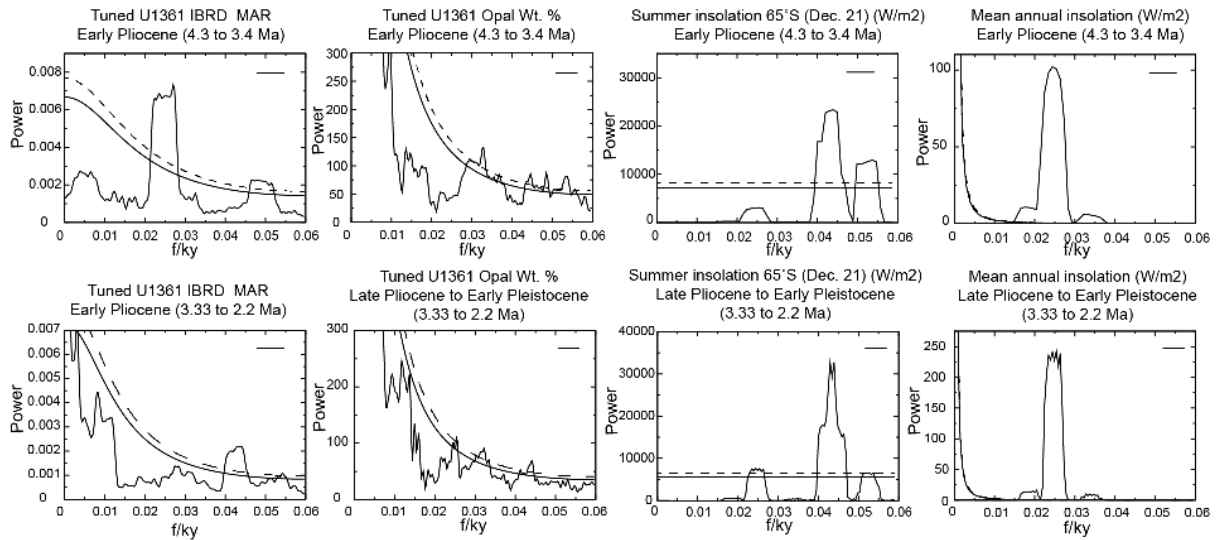**Extended Data Figure 6. Power spectra using Robust and Raw AR(1) red noise background.** Raw data output is represented in black lines, while harmonic reshaping data output set to a 90% threshold is represented with green lines in which red lines highlight harmonics. Statistical significance is noted at 90% (solid black line) and 95% (dashed black line).

831

832

Extended Data Figure 7. Power spectra using the IBRD tuned age model. Early Pliocene

IBRD MAR and mean annual insolation display strong 40 kyr cycles of obliquity while

biogenic opal does not display Milankovitch orbital frequencies. Late Pliocene-Early

Pleistocene IBRD MAR and summer insolation display strong 23 and 19 kyr cycles of

precession while biogenic opal wt. % only contains less distinct precession frequencies with

40 kyr obliquity significance. Statistical significance is noted at 90% (solid black line) and

95% (dashed black line).

840

Extended Data Table 2. Antarctic-Arctic[28] precession-paced climate phase relationship.

Synchronised by the timing of the top and bottom Kaena Subchron paleomagnetic reversals.

P-mag boundary	Age (Ma)	Insolation 65°N (w/m2)	Insolation 65°S (w/m2)	U1361 Wilkes Land proxy	Antarctic U1361 climate	Lake El'gygytgyn proxy	Arctic Lake E climate
Top Kaena	3.032	Low (443.24)	High (535.22)	Peak opal* Peak Ba/Al High IBRD* Diatom-rich*	Sea-ice free, productive warm open ocean during summer with ice berg rafting	Low opal Low Si/Ti Low trees and shrubs index* Low MTWM* Low precipitation index	Cool, dry summers Low lake productivity Cold deciduous forest
Base Kaena	3.116	High (509.84)	Low (479.43)	Low opal* Low Ba/Al Low IBRD* Diatom-poor*	Sea-ice covered, non-productive cold ocean during summer with limited ice berg rafting	High opal High Si/Ti High trees and shrubs Index* High MTWM* Increased precipitation index	Warmer, wetter summers Increased lake productivity Cool conifer mixed forest

843
844 * Data displayed in Fig. 3a.

845

846

847
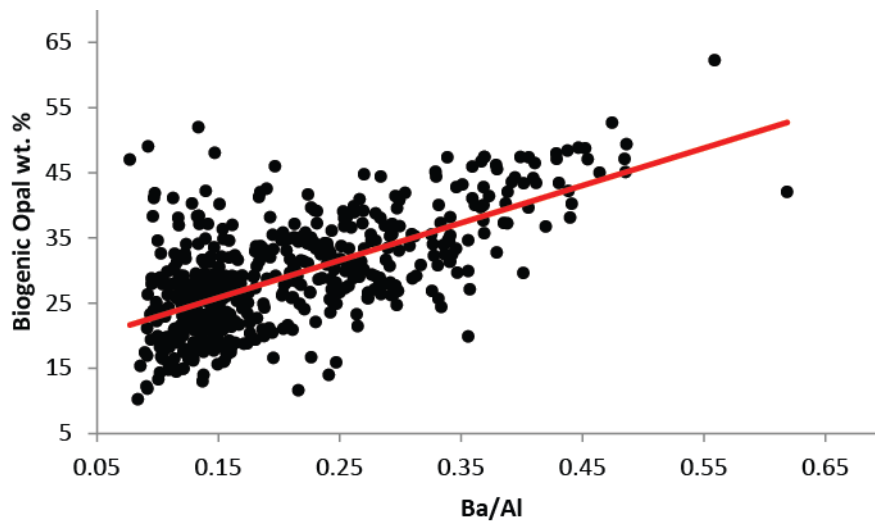
Extended Data Figure 8. Cross plot of U1361 biogenic opal wt. % and Ba/Al. Linear

interpolated at 3 kyr resolution of biogenic opal wt. % and Ba/Al with r = 0.65 and p value of

0.00.

851

Supplementary References

32. Krissek, L, A. 11. Late Cenozoic ice-rafting records from Leg 145 sites in the north

Pacfic: Late Miocene onset, Late Pliocene intensification and Pliocene-Pleistocene events.

Proc. Ocean Drill. Program, Sci. Results **145**, 179-194 (1995).

856

33. Ghil, M. et al. Advanced spectral methods for climatic time series. *Rev. Geophys.* **40**(1),

(2002).

859

34. Mann, M. E., & Lees, J. M. Robust estimation of background noise and signal detection

in climatic time series. *Climatic Change* **33**(3), 409-445 (1996).

862

863   35. Cowan, E. A., Hillenbrand, C-D., Hasslet L. E., & Ake, M. T. Coarse-grained terrigenous

864   sediment deoposition on continental rise drifts: A record of Plio-Pleistocene glaciation on the

865   Antarctic Peninsula. *Palaeogeogr. Palaeoclimatol. Palaeoecol.* **265**(3-4), 275-291 (2008).

866

867   36. Sperazza, M., Moore, J. N., & Hendrix, M. S. High-resolution particle size analysis of

868   naturally occurring very fine-grained sediment through laser diffractometry. *J. Sediment. Res.*

869   **74**(5), 736-743 (2004).

870

871   37. Escutia, C., Brinkhuis, H., Klaus, A., & Expedition 318 Scientists. Site U1361. *Proc.*

872   *Integrat. Ocean Drill. Program* **318**, 1-57 (2011).

873

874   38. Folk, R. L., & Ward, W. C. Brazos River bar [Texas]; a study in the significance of grain

875   size parameters. *J. Sediment. Res.* **27**, 3-26 (1957).

876

877   39. Passchier, S. Linkage between East Antarctic Ice Sheet extent and Southern Ocean

878   temperatures based on Pliocene high-resolution record of ice-rafted debris off Prdyz Bay,

879   East Antarctica, *Paleoceanography* **26,** (2011).

880

881   40. Bindoff, N. L., Rosenberg, M. A., & Warner, M. J. On the circulation and water masses

882   over the Antarctic continental slope and rise between 80 and 150°E. *Deep Sea Res. II* **47**(12-

883   13), 2299-2326 (2000).

884

885   41. McCave, I. N., & Hall, I. R. Size sorting in marine muds: Processes, pitfalls, and

886   prospects for paleoflow-speed proxies. *Geochem. Geophys. Geosyst.* **7**(10), 1-37 (2006).

887

888   42. Escutia, C. et al. Cenozoic ice sheet history from east Antarctic Wilkes Land continental

889   margin sediments. *Global Planet. Change* **45**(1-3), 51-81 (2005).

890

891   43. Caburlotto, A. et al. Sedimentary processes on the Wilkes Land continental rise reflect

892   changes in glacial dynamic and bottom water flow. *Int. J. Earth Sci.* **99**, 909-926 (2010).

893

894   44. Ó'Cofaigh, C., Dowdeswell, J. A., & Pudsey, C. J. Late Quaternary iceberg rafting along

895   the Antarctic Peninsula continental rise and in the Weddell and Scotia Seas. *Quaternary*

896   *Research* **56**(3), 308-321 (2001).

897

898   45. Anderson, J. B. *Antarctic Marine Geology*. Cambridge University Press, Cambridge.

899   (1999).

900

901   46. Stuart, K. M., & Long, D. G. Tracking large tabular icebergs using the SeaWinds Ku-

902   band microwave scatterometer. *Deep Sea Res. Part II* **58**(11), 1285-1300 (2011).

903

904   47. Paillard, D, Labeyrie, L., & Yiou, P. Macintosh program performs time-series

905   analysis. *Eos, Trans. Amer. Geophys. Union* **77**(39), 379 (1996).

906

907   48. Dymond, J., Suess, E. and Lyle, M. Barium in deep-sea sediment: a geochemical proxy

908   for paleoproductivity. *Paleoceanography* **7**(2), 163-182 (1992).

909

910   49. Stow, D. A. V., & Piper, D. J. W. Deep-water fine grained sedimentsL facies models, in

911   Fine-Grained Sediments: Deep-Water Processes and Facies. *Geol. Soc. Spec. Publ.,* **15**(1),

912   611-646 (1984).

913

914   50. Gilbert, I. M., Pudsey, C. J., & Murray, J. W. A sediment record of cyclic bottom-current

915   variability from the northwest Weddell Sea. *Sedimentary geology* **115**(1), 185-214 *(*1998).

916

917   51. Pudsey, C. J., & Camerlenghi, A. Glacial–interglacial deposition on a sediment drift on

918   the Pacific margin of the Antarctic Peninsula. *Antarctic Science* **10**, 286-308 (1998).

919

920   52. Pudsey, C. J. Sedimentation on the continental rise west of the Antarctic Peninsula over

921   the last three glacial cycles. *Marine Geology* **167**(3), 313-338 (2000).

922

923   53. Busetti, M. et al. Plio-Quaternary sedimentation on the Wilkes land continental rise:

924   preliminary results. *Deep Sea Res. Part II* **50**(8-9), 1529-1562 (2003).

925

926   54. Hepp, D. A., Mörz, T., & Grützner, J. Pliocene glacial cyclicity in a deep-sea sediment

927   drift (Antarctic Peninsula Pacific Margin). *Palaeogeogr. Palaeoclimat. Palaeoecol.* **231**, 181-

928   198 (2006).

929

930   55. Lucchi, R. G., & Rebesco, M. Glacial contourites on the Antarctic Peninsula margin:

931   insight for palaeoenvironmental and palaeoclimatic conditions. *Geol. Soc. London Spec.*

932   *Publ.* **276**(1), 111-127 (2007).

933

934   56. Escutia, C., Eittreim, S. L., & Cooper, A. Cenozoic glaciomarine sequences on the Wilkes

935   Land continental rise, Antarctica. *VII International Symposium on Antarctic Earth Sciences*

936   *Proceedings Volume* 791–795 (1997).

937

938   57. Escutia, C., et al. Current controlled deposition on the Wilkes Land continental rise,

939   Antarctica. *Geol. Soc. London Mem.* **22**(1), 373-384 (2002).

940

941   58. Donda, F., Brancolini, G., De Santis, L., & Trincardi, F. Seismic facies and sedimentary

942   processes on the continental rise off Wilkes Land (East Antarctica): evidence of bottom

943   current activity. *Deep Sea Res. Part II: Top. Stud. Oceanogr.* **50**(8-9), 1509-1527 (2003).

944

945   59. Hesse, R. et al. Asymmetrical turbid surface-plume deposition near ice-outlets of the

946   Pleistocene Laurentide ice sheet in the Labrador Sea. *Geo-Marine Letters* **17**(3), 179-187

947   (1997).

948

949   60. Beaman, R. J., O'Brien, P. E., Post, A. L., & De Santis, L. A New High-Resolution

950   Bathymetry Model for the Terre Adélie and George V Continental Margin, East Antarctica.

951   *Antarctic Science* **23**(1), 95–103 (2011).

952

953   61. Cooper, A. K., Barrett, P. J., Hinz, K., Traube, V., Letichenkov, G., & Stagg, H. M. J.

954   Cenozoic prodrading sequences of the Antarctic continental margin: a record of glacio-

955   eustatic and tectonic events. *Marine Geology* **102**, 175-213 (1991).

956

957   62. Rebesco, M., & Camerlenghi, A. Late Pliocene margin development and mega debris

958   flow deposits on the Antarctic continental margins, Evidence of the onset of modern

959   Antarctic Ice Sheet? *Palaeogeogr. Palaeoclimat. Palaeoecol.* **260**(1-2), 149–167 (2008).

960

961   63. Presti, M., De Santis, L., Busetti, M., & Harris, P. T. Late Pleistocene and Holocene

962   sedimentation on the George V Continental Shelf, East Antarctica. *Deep Sea Res. Part II*

963   **50**(8-9) 1441-1461 (2003).

964

965   64. Orsi, A. H., Whitworth, T., & Nowlin, W. D. On the meridional extent and fronts of the

966   Antarctic Circumpolar Current. *Deep Sea Res. Part I* **42**(5), 641-673 (1995).

967

968   65. Dowsett, H. J. et al. Assessing confidence in Pliocene sea surface temperatures to

969   evaluate predictive models. *Nature Clim. Change* **2**(5), 365-371 (2012).

970

971   66. Whitehead, J. M., & Bohaty, S. M. Pliocene summer sea surface temperature

972   reconstruction using silicoflagellates from Southern Ocean Site 1165. *Paleoceanography*

973   **18**(3), (2003).

974

975   67. Hillenbrand, C., and Cortese, G. Polar stratification: A critical view from the Southern

976   Ocean. *Palaeogeogr. Palaeoclimat. Palaeoecol.* **242**(3-4), 240-252 (2006).

977

978   68. Denton, G. H., et al. The last glacial termination. *Science* **328**(5986), 1652-1656 (2010).

979

980   69. Williams, G. D., & Bindoff, N. L. Wintertime oceanography of the Adélie

981   Depression. *Deep Sea Res. Part II* **50**(8), 1373-1392 (2003).

982